



## Geophysical and geotechnical properties of near-seafloor sediments in the northern Gulf of Mexico gas hydrate province

F. Francisca<sup>1</sup>, T.-S. Yun, C. Ruppel<sup>\*</sup>, J.C. Santamarina<sup>2</sup>

*Georgia Institute of Technology, Atlanta, GA 30332, United States*

Received 24 September 2004; accepted 2 June 2005

Available online 9 August 2005

Editor: E. Boyle

### Abstract

Relatively few studies have focused on the geotechnical properties of near-seafloor (uppermost 10 m) sediments that are encountered during shallow coring or the initial phases of seafloor drilling. Such sediments are of particular interest in areas strongly affected by salt tectonics or the occurrence of shallow gas hydrates. Using sediment cores obtained at three gas hydrate and/or mud volcano sites in the northern Gulf of Mexico (Garden Banks GB425, Mississippi Canyon MC852, and Green Canyon GC185), we report on visual observations of gas hydrate, oil, and authigenic carbonates; index properties (grain size characteristics, specific surface, pH, Atterberg limits, water content/porosity); small-strain (shear wave velocity) and large-strain (undrained shear strength) mechanical properties; and electrical properties (dielectric permittivity, electrical conductivity). At all sites, sediments are dominated by clay minerals (probably illite) and the highest proportion of carbonate (up to 72%) occurs near the apparent central vent of the mud mound at MC852. Based on the synthesis of several types of data, we conclude that the strength, stiffness, and porosity of the near-seafloor sediments are governed not by overburden vertical effective stress, but rather by interparticle forces arising from the interaction of the ionic pore fluid with the high specific surface ( $53$  to  $76 \text{ m}^2 \text{ g}^{-1}$ ) sediment grains. In some of the shallow sediments, pore water ionic concentrations significantly exceed seawater, suggesting transport of brines from deeper salt bodies. Particle-level processes, including those associated with these high ionic concentrations, lead to a mechanistic explanation for the moussey sediment texture widely observed in cores that have experienced the dissociation of gas hydrates. Electrical conductivity measurements acquired at millimeter resolution near dissociating gas hydrate indicate that, prior to hydrate dissociation, the pore fluids are in equilibrium with those distal from the hydrate.

© 2005 Elsevier B.V. All rights reserved.

*Keywords:* gas hydrate; marine sediment; mechanical properties; Gulf of Mexico; electrical properties

<sup>\*</sup> Corresponding author. School of Earth and Atmospheric Sciences, Georgia Tech, 311 Ferst Dr., Atlanta, GA 30332-0340, United States. Tel.: +1 703 292 7575; fax: +1 703 292 9085.

*E-mail addresses:* [ffrancis@gtwing.efn.uncor.edu](mailto:ffrancis@gtwing.efn.uncor.edu) (F. Francisca), [cdr@eas.gatech.edu](mailto:cdr@eas.gatech.edu) (C. Ruppel), [carlos@ce.gatech.edu](mailto:carlos@ce.gatech.edu) (J.C. Santamarina).

<sup>1</sup> Current address. Universidad Nacional de Cordoba-CONICET, Facultad de Ingenieria, Av. Vélez Sarsfield 1601 Córdoba 5016, Argentina. Tel.: +54 351 156534710.

<sup>2</sup> Tel.: +1 404 894 7605.

## 1. Introduction

Despite its origin as a passive continental margin, the Gulf of Mexico is a tectonically-active and geologically complex environment characterized by faulting, folding, and other deformational processes that largely arise due to the layering of thick sedimentary sequences over buoyant salt deposits. The evolution of the salt domes and associated salt withdrawal basins contributes to the development of faults that serve as conduits for migrating fluids, including gases, liquid hydrocarbons, and brines.

The migration of free gas and of fluids with large concentrations of dissolved gases leads to the formation of gas hydrates. An unusual feature of the shallow-water part of the Gulf of Mexico is the occurrence of gas hydrates as seafloor mounds (e.g., [1,2]) and in sediments shallow enough to be accessible by piston coring (5 to 20 m). The resulting distribution of gas hydrates contrasts with that in many other continental margins (e.g., Blake Ridge, Costa Rica margin, Cascadia and Nankai accretionary margins), where the top of the methane gas hydrate zone lies tens of meters to more than a hundred meters below the seafloor due to a combination of gas solubility and gas supply constraints [3].

Several factors lead to hydrate formation at and near the seafloor in parts of the Gulf of Mexico. Gas hydrate stability conditions depend primarily on pressure, temperature, and the composition of the host gas. Secondary factors affecting hydrate stability include salinity and sediment composition. In areas dominated by salt tectonics (e.g., northern Gulf of Mexico), the presence of high salinity pore fluids alter the gas hydrate stability zone due to both the high thermal conductivity of salt and the inhibitory effect of dissolved salt on hydrate formation [4–6]. Such thermal and chemical perturbations, which are particularly prevalent above and on the flanks of salt diapirs, tend to compress the gas hydrate zone closer to the seafloor. The rate, amount, and composition of the gas supply and the absence or presence of microbially-mediated oxidation and reduction reactions in shallow sediments also affect the availability of methane to produce hydrate near the seafloor. In particular, at water depths greater than ~500 m, the sulfate reduction zone is sometimes thin or absent, and gas hydrate may occur at or near the seafloor at

vents that mark the loci of rapid gas and fluid advection (e.g., [7]).

Although academic drilling and some industry research have characterized the deeper part of the sedimentary section in a number of gas hydrate provinces, only a few researchers (e.g., [8–12]) have focused on the physical properties of near-seafloor Gulf of Mexico sediments that may host gas hydrates. Studies of near-seafloor sediments have relevance not only for understanding the interaction of gas hydrate with high porosity and mechanically weak near-seafloor sediments, but also for elucidating the properties of sediments (with and without hydrate) encountered at the outset during drilling and coring efforts. In this study, we measure geophysical and geomechanical properties of near-seafloor (uppermost 4 m) sediment cores recovered from several sites in the Gulf of Mexico. Special emphasis is placed on the systematic description of gas hydrates and hydrocarbons and their interaction with the sediments.

## 2. Study sites

This study investigates sediments recovered in piston and gravity cores acquired at 3 shallow-water (<1100 m water depth) Gulf of Mexico sites aboard the *R/V Seward Johnson* in October 2002. The sites, shown in Fig. 1, were chosen to meet objectives related to quantifying fluid, gas, and heat flux at hydrates-related sites (e.g., [14]) and have previously been described by several workers (e.g., [2,6,7,15,16]). The study sites are loci for expulsion of thermogenic and/or biogenic gas, the emission of liquid hydrocarbons, the precipitation of authigenic carbonate, and, in some cases, the formation of gas hydrates. All sites lie within the salt mini-basin physiographic provinces defined by [17].

The Green Canyon (GC) site is located at Bush Hill near Jolliet Field in lease block GC185 at an average water depth of ~540 m and has been the subject of extensive studies for more than 2 decades [1,2,7,13,18–20]. (Throughout this paper, lease block designators are used to refer to the specific study area within the lease block, not to the characteristics of the lease block as a whole.) Bush Hill is an asymmetric, acoustically transparent mud mound that measures ~0.5 km wide by up to 1 km long and ~40 m high

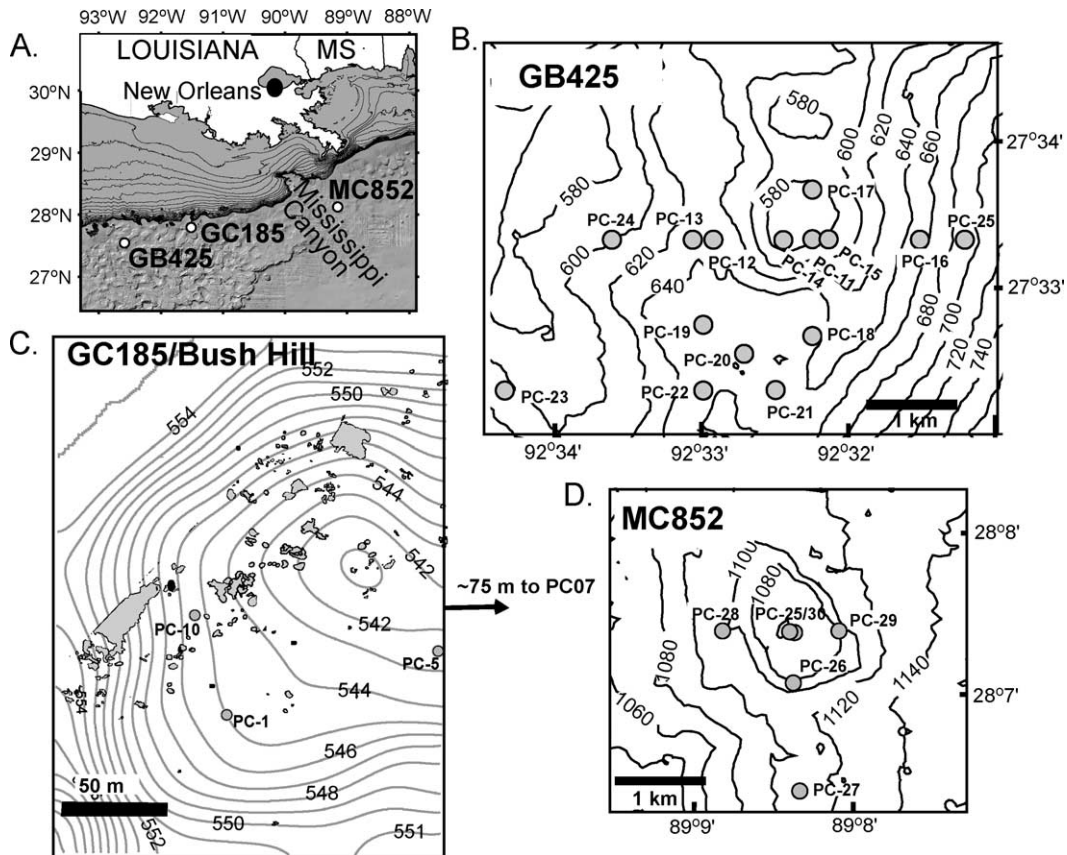


Fig. 1. (A) Location map showing the U.S. Gulf Coast and the three study sites. (B) Garden Banks 425 with piston core locations. The main mud volcano edifice is located near PC-11. All contours are in meters. (C) Green Canyon 185, also known as Bush Hill. Only the cores discussed in the paper are shown here. Gray areas denote carbonate hardgrounds from [13]. (D) Mississippi Canyon site, which lies at the border between lease blocks 852 and 853 and which is referred to as MC852 throughout this paper. Mud volcano central vent coincides with PC-25.

[e.g., 18]. The feature is located at the intersection of two faults associated with seeping oil and gas, hardgrounds of authigenic carbonate, and significant chemosynthetic communities, particularly tubeworms and bacterial mats [e.g., 20]. Gas hydrates occur in mounds on the seafloor close to gas vents and are usually covered by a thin layer of sulfide-rich sediments or oil [2]. Expelled gas is mostly methane, with some ethane and lesser quantities of other gases [2], and the near-seafloor sediments contain oil, dispersed hydrate nodules, carbonates, and abundant hydrogen sulfide.

The Garden Bank 425 site (GB425) lies at an average water depth of ~620 m and is the locus of a ~30-m-high mud mound [21] and an active brine

pool. Sidescan sonar data [7] and Chirp images collected during our 2002 cruise reveal stratigraphic relationships that may be consistent with recent mudflows near the vents, and at least one subsidiary vent is readily identifiable at the site [7]. Fractures related to deformation that accommodated rising, buoyant salt bodies [22] facilitate the vertical migration of oil and gas from the deep reservoir. Chemosynthetic communities (mussels) are not well-developed compared to GC185 [13]. Workers have reported gas hydrate at this location [13] and an authigenic carbonate cap on the summit of the mud mound feature [15].

The Mississippi Canyon site lies at average water depth of 1080 m along the boundary between lease

blocks MC852 and MC853, north of the Ursa field. The site includes a 1.5-km-wide apparent mud volcano that rises ~30 m above the surrounding seafloor, which appears from Chirp profiles to be normally sedimented and not overlain by recent mudflows. Fluid migration from the subsurface hydrocarbon reservoir occurs through fractures associated with a salt body at depth ([22]; P. Flemings, personal communication, 2005). We recovered gas hydrate from this location in 2002 [6], and previous investigators reported that the sediments at this site contain thermogenic gas hydrates and carbonates, and biodegraded crude oil [19].

### 3. Sampling strategy

The location, recovered length, and other characteristics of cores from which sediment samples were obtained are summarized in Table 1. None of the recovered cores reached the anticipated 5 to 10 m length, due primarily to problems with the shipboard coring rig and occasionally to the presence of indurated layers or carbonates. In some cases, the piston corer was operated as a gravity corer due to problems with the piston. For consistency with [6] and to distinguish between the true gravity corer and the longer piston core rig, these cores retain the designation “PC”

Table 1  
Core locations and characteristics

Core number <sup>a</sup>	Latitude (N)	Longitude (W)	Water depth (m)	Length (m)	Hydrate	Carbonate	Oil or gas
<i>Green Canyon (Bush Hill: GC185)</i>							
PC 01	27°44.502	91°19.088	537	3.5	•	•	•
GC 04a	27°46.931	91°30.486	535	1.0			•
GC 04b	27°46.926	91°30.492	537	0.72			
PC 01b	27°46.912	91°30.493	538	1.33	•		•
PC 02	27°46.921	91°30.479	535	3.10			•
PC 05	27°46.928	91°30.440	534	5.73	•		•
PC 06	27°46.927	91°30.471	536	1.48			
PC 07b	27°46.940	91°30.401	538	1.95		•	
PC 10	27°46.937	91°30.501	537	2.63		•	•
<i>Garden Banks (GB 425)</i>							
PC 11a	27°33.349	92°32.700	564	1.16			•
PC 12	27°33.310	92°32.945	625	2.11			
PC 13	27°33.309	92°32.088	627	3.06		•	
PC 14	27°33.299	92°32.399	564	2.39		•	•
PC 15	27°33.347	92°32.087	569	2.25			
PC 17	27°33.640	92°32.221	566	2.35			
PC 18	27°32.642	92°32.227	639	2.67		•	
PC 19b	27°32.727	92°32.956	647	3.48			
PC 20	27°32.579	92°32.447	652	1.95			
PC 21	27°32.274	92°32.482	642	3.70		•	•
PC 22	27°32.269	92°32.956	650	3.67		•	•
PC 23	27°32.270	92°32.302	587	1.82			
GC 7	27°33.214	92°32.318	567	1.1			
PC 24b	27°33.291	92°32.598	574	2.9		•	
<i>Mississippi Canyon (MC852)</i>							
PC 25	28°7.380	89°8.381	1067	1.81	•	•	
PC 26	28°7.065	89°8.386	1083	2.74		•	•
PC 27	28°6.393	89°8.350	1098	4.02			
PC 28	28°7.388	89°8.827	1093	1.64			
PC 29	28°7.389	89°8.104	1068	2.8			
PC 30	28°7.385	89°8.409	1070	3.56	•	•	•

<sup>a</sup> GC denotes gravity cores, and PC represents long piston cores collected in the piston coring apparatus, even when the piston was not used.

in Table 1 and throughout this study. The time between removal of the coring apparatus from the seafloor to commencement of shipboard laboratory testing detailed here ranged from 40 to 120 min. For this research, we used whole round sections 0.07 to 0.1 m long collected at 0.3 to 0.5 m intervals from some of the recovered cores.

Nearly every core was scanned with an infrared camera immediately upon recovery in an effort to detect colder regions associated with the endothermic dissociation of gas hydrate (J. Weinberger, personal communication). Core sections that contained gas hydrate were sampled and tested before samples lacking hydrate, but relatively few cores reached the ship's deck with intact gas hydrate.

#### 4. Results

The following sections incorporate both the test procedures and the results for various visual, index, mechanical, and electrical properties. Table 2 summarizes the laboratory tests conducted shipboard immediately after core recovery and in facilities at the Georgia Institute of Technology after the cruise.

Table 2  
Geotechnical tests conducted on recovered sediments

Properties	Method
<i>Shipboard measurements</i>	
Shear wave velocity ( $V_s$ )	Bender element
Undrained shear strength ( $S_u$ )	Pocket torvane (ASTM D 4648) [39]
Conductivity ( $\sigma$ )	Needle probe
pH	pH strip
<i>Post-cruise laboratory measurements</i>	
Water content	Oven-drying (ASTM D 2216) [31]
Conductivity ( $\sigma_{ci}$ ) of pore fluid	Needle probe
Specific surface ( $S_s$ )	Methylene blue adsorption
Grain size distribution	Sieve and hydrometer (ASTM D 422-63) [27] (ASTM D 4318) [35]
Atterberg limits (LL/PL)	Reflection-coaxial termination probe
Complex permittivity	Acid reaction (ASTM D 4373) [31]
Carbonate content	

#### 4.1. Visual and optical microscopy

Oil and gas that likely migrated from depths of several kilometers [21] were found within the recovered sediments at all three sites (Table 1). The oil formed droplets (dispersed phase) or seams (percolating phase) and accumulated at interfaces where migration was hindered by shells or carbonates. All primary oil seams observed in the samples were oriented vertically, and the sediment could be peeled off along these seams. Cores probably experienced only ~1% strain [23], making it unlikely that these vertically oriented seams were a consequence of coring.

The oil is of medium–heavy viscosity at room temperature, and a single drop can be stretched to form long strings (>200 mm). When oil-covered shells were removed from the sediment and immersed in water, the oil film rapidly breaks, allowing the water to reach the mineral surface. Likewise, a fresh sediment surface immersed in water experienced rapid dispersion of the clay around the oil, exposing the droplets. Based on these observations, we conclude that shells and mineral particles in these young sediments remain water wet and oleophobic.

Hydrate-bearing sediments were recovered at GC185 and at the apparent central mud volcano vent at MC852 (Table 1). Hydrate lenses in Green Canyon sediments were found within oil seams, with all faces of the lenses coated with oil in every observed occurrence. The largest and most persistent oil seam was oriented vertically and filled with a continuous methane hydrate lens that ran across the core (7 cm diameter) for more than 40 cm of the core's length. At MC852, the hydrate was associated not with visible oil seam, but with carbonate, which occurred as both granular and aggregate material. The hydrate was recovered from ~2.5 m below the seafloor, and the cores smelled strongly of kerosene despite the absence of visible oil.

The importance of microbially-mediated sediment diagenesis is manifested in near-surface Gulf of Mexico sediments by the presence of authigenic carbonates, both as small nodules and sedimentary zones within cores and at the larger scale of carbonate hardgrounds [24,25]. Thin authigenic carbonate layers were encountered in several of the cores at each of the 3 study sites (Table 1). An authigenic carbonate specimen from GC185 was a lithified plate ~70 mm

on the side and ~5 mm thick, with several tubular “chimneys” protruding from the plate. The largest chimney, which may represent a carbonate-lined polychaete burrow, had length 15 mm, O.D. 11 mm, and I.D. 3.5 mm, much smaller than true carbonate chimneys reported in other provinces (e.g., Gulf of Cadiz [26]). Carbonate specimens recovered inside cores had rough surfaces, cavities, and high internal porosity, and they disaggregated along preexisting discontinuities when handled. Observations were consistent with the gradual agglomeration of carbonate combined with cavity expansion within the soft sediment. Sporadic and small thin wedges on the periphery suggested limited growth by fracturing of the surrounding sediment.

#### 4.2. Index properties

Specimens were tested to determine the grain size distribution, specific surface, carbonate content, pH, and consistency limits.

##### 4.2.1. Grain size distribution

The grain size distribution was determined for representative cores at each site. Sieve analyses were used for the coarser portion, while sedimentation columns and hydrometer tests were applied for the fine portion passing sieve #40 [27]. The grain size distribution curves shown in Fig. 2A and summarized in Table 3 reveal that more than 48% of the sediment is of clay size (<2  $\mu\text{m}$ ) at each site, while less than 5% of the sediment is within the sand range (>75  $\mu\text{m}$ ).

Table 3

Index values and soil classification

Properties	Sites		
	GC185	GB425	MC852
Sand fraction (>75 $\mu\text{m}$ ) (%)	4.9	2.6	3.5
Clay fraction (<2 $\mu\text{m}$ ) (%)	55.0	52.5	48.5
Specific surface range ( $\text{m}^2/\text{g}$ )	57–79	53–88	30–64
Carbonate range (%)	4–55	6–35	7–72
Liquid limit, LL	102.4	72.1	55.4
Plastic limit, PL	45.3	29.9	27.8
Activity	1.0	0.8	0.6
United Soil Classification	OH or MH	OH or MH	CH

The GB425 mud volcano site had more fine-grained material (clay and fine silt) than either Bush Hill (GC185) or the MC852 mud volcano, which is located within the more variegated sediments of the distal part of the Mississippi River outwash plain.

##### 4.2.2. Specific surface

The specific surface  $S_s$  of mineral grains is a measure of the smallest dimension of the grain, which corresponds to the radius of spherical particles and to the particle thickness in platy clay particles. In clays, the specific surface is a good indicator of mineralogy, and laboratory experiments with synthetic gas hydrate have demonstrated that specific surface plays an important role in determining the mechanical and electrical properties of hydrate-bearing sediments [28]. The variation in specific surface with depth of recovered sediments was determined in one core from each site using the methylene blue absorption technique, which can more adequately assess swelling

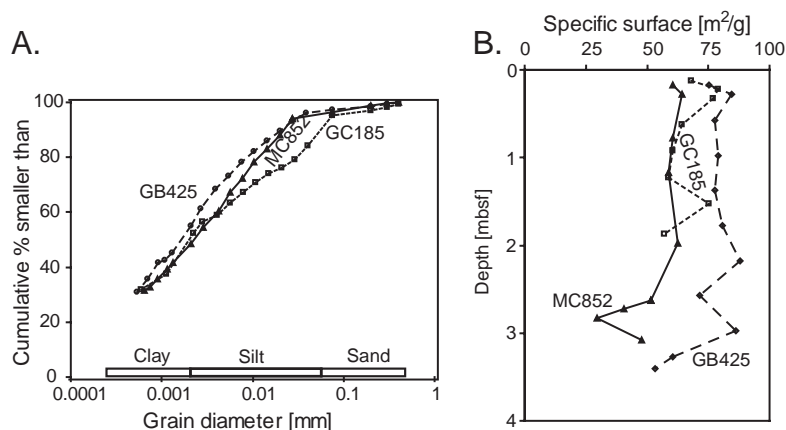


Fig. 2. (A) Grain size distribution and (B) specific surface for one core at each site. Depth unit denotes meters below seafloor.

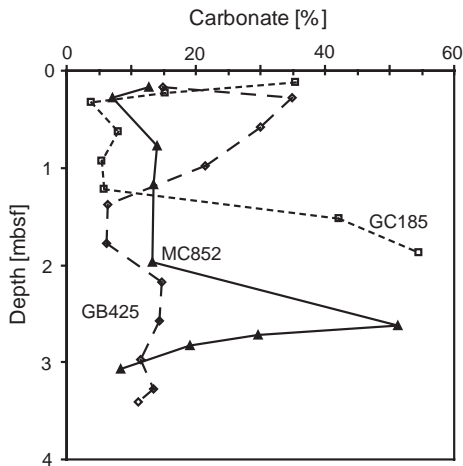


Fig. 3. Percentage of carbonate based on the dry weight of sediments for a representative core at each site.

minerals than dry methods such as gas adsorption [29]. The results, summarized in Fig. 2B, vary from  $S_s \cong 40 \text{ m}^2 \text{ g}^{-1}$  to  $S_s \cong 90 \text{ m}^2 \text{ g}^{-1}$ , a range consistent with illite ( $S_s=65$  to  $100 \text{ m}^2 \text{ g}^{-1}$  [30]). Independent analyses that applied X-ray diffraction to a group of longer (~10–15 m) cores from the Gulf of Mexico also yielded illite as the dominant clay mineral [8]. The average specific surface of the MC852 sediments (PC-30;  $\bar{S}_s=53 \text{ m}^2 \text{ g}^{-1}$ ) was smaller than that at the other two sites ( $\bar{S}_s=76 \text{ m}^2 \text{ g}^{-1}$  for GB425 (PC-19) and  $\bar{S}_s=67 \text{ m}^2 \text{ g}^{-1}$  for GC185 (PC-7b)), but the values were not as low as would be expected if kaolinite were the predominant constituent.

#### 4.2.3. Carbonate content

Carbonate content was measured using ASTM protocol D4373-02 [31], which is based on the chemical reaction of the carbonate with hydrochloric acid. The pressure increase related to the generation of carbon dioxide ( $\text{CaCO}_3 + 2\text{HCl} \rightarrow \text{CO}_2 + \text{Cl}_2\text{Ca} + \text{H}_2\text{O}$  for calcium carbonate) is measured in a closed 1-l Plexiglas cell. Prior to testing, the cell is calibrated to determine the pressure-versus-carbonate content function. The time required to reach stable pressure ranges from 1 to 10 min, with longer equilibration times necessary when dolomites ( $\text{MgCO}_3$ ) are present.

Fig. 3 shows carbonate content versus depth for a single carbonate-bearing core from each of the three study sites. The high spatial variability suggests a localization-type formation process. Carbonate con-

tent varied from 4% to 55% at GC185 (PC-7), 6% to 35% at GB425 (PC-19), and 7% to 72% at MC852 (PC-30) along the cores, which were not always sampled at equal intervals. Due to the relationships among authigenic carbonate formation, microbial activity, methane production, and gas hydrates [e.g., 25], the distribution of carbonate near vent sites should have significance for the vigor of fluid and gas flux. However, the limited data prevent us from drawing further conclusions. For the 3 cores analyzed, the discrete depth (~2.6 mbsf in PC-30 from MC852) at which maximum carbonate was observed coincided with the occurrence of gas hydrate.

#### 4.2.4. pH

The pH was measured on freshly exposed surfaces near the center of cores using a non-bleeding, pH-sensitive strip applied immediately following core splitting. The estimated precision of these measurements is  $\pm 0.25$ . The pH data shown in Fig. 4 indicate relatively stable values throughout the uppermost few meters of sediment for individual cores, and appreciable lateral variability at each study site. pH was significantly lower near mud volcano vents (7.5 at PC-17 at GB425; 7.8 and 8.0 at PC-25 and PC-30, respectively, at MC852) than at distal reference sites

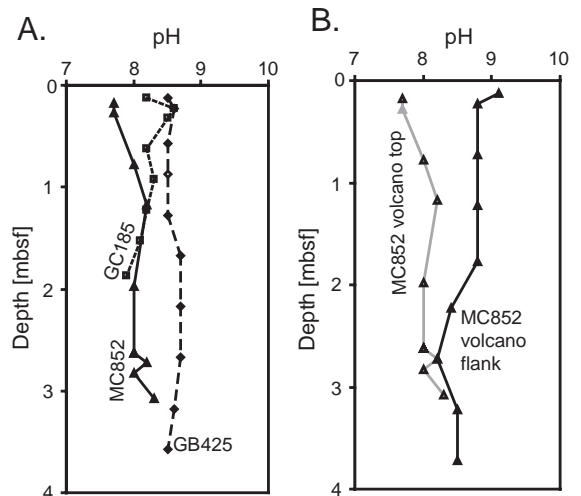


Fig. 4. (A) pH for representative cores at each site and (B) a comparison of pH at the top of the MC852 mud volcano and on its flank. pH is significantly lower on top of the volcano.

(8.3 at GB425; 8.7 to 9.1 for 3 cores at MC852). Carbonate and bicarbonate precipitation within the sulfate reduction zone causes alkalinity to increase [32], while carbonate dissolution is associated with a lower pH environment. The observed patterns of pH variability are consistent with net carbonate precipitation in areas distal from the vents and net dissolution near areas of peak energy, fluid, and gas flux at vents. Where pH was tested proximal to gas hydrates, we noted lower pH (7.5 and 7.8) in hydrate-bearing sediments compared to pH of greater than 8.1 for reference sediments at GC185.

#### 4.2.5. Water content and porosity

The gravimetric water content  $w$  was determined by drying specimens at 105 °C (ASTM D2216 [33]). In general, water content is expected to decrease with depth when compaction keeps pace with sedimentation. In contrast, sediments that are cemented faster than the rate of deposition typically have constant water content with depth [34].

Representative water content profiles and data are shown in Fig. 5 and Table 4. The down-core profiles indicate a slight decrease in water content with depth. In general, cores collected at and proximal to the mud volcano vents at sites GB425 and MC852 had sig-

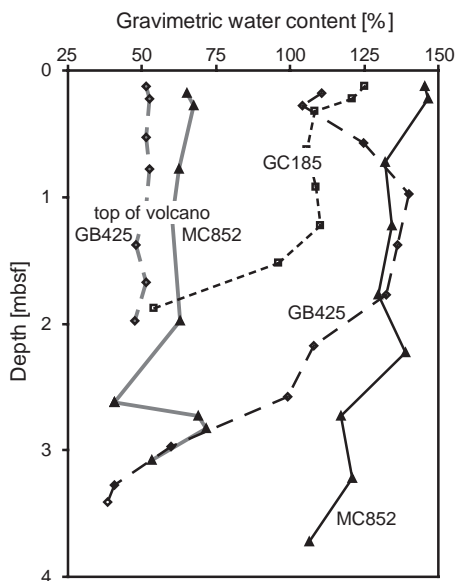


Fig. 5. Water content for representative cores at the sites and for cores proximal to the locus of mud venting.

nificantly lower average water content ( $< \sim 70\%$ ) than those recovered from locations more distal from the vents ( $> \sim 80\%$ ). For the most part, the cores with lower water content were the same ones in which pore fluids had significantly higher conductivity, corresponding to higher ionic concentrations (see below). The water content and pore water salinity vary so dramatically in the vicinity of the mud volcanoes that these parameters can be used as diagnostics for determining the locus of most active venting of formation fluids.

The water content  $w$  of sediments can be converted to porosity  $n$  if the specific gravity  $G_s$  of the minerals and the degree of saturation  $S$  are known:  $G_s \cdot w = S \cdot n / (1 - n)$ . Using 100% saturation and assuming specific gravity corresponding to grain density of 2650 kg/m<sup>3</sup>, we calculated the sediment porosity. Fig. 6 shows the complete porosity database compiled for the cores, with data points distinguished according to the electrical conductivity of the pore fluid. The populations of high porosity–lower conductivity pore fluid and lower porosity–higher conductivity pore fluid naturally separate in this analysis. These results suggest that interparticle electrical forces (double layer repulsion and van der Waals) are more important than effective stress in controlling the porosity of these high specific surface sediments at low confinement. Some of the porosity variability encapsulated in Fig. 6 may reflect complications associated with the determination of the true depth of sediments along the core (i.e., soft sediments are displaced during piston coring or lost during gravity coring), the presence of gas bubbles that cause sediments to be locally unsaturated, and/or the presence of oil, most of which is volatilized during drying.

#### 4.2.6. Atterberg limits and soil classification

The Atterberg liquid limit (LL) and plastic limit (PL) are the water contents associated with changes in soil rheological behavior and are often used in the classification of fine-grained sediments. The liquid limit and plastic limit correspond to the water contents at which the soil–water mixture undergoes transition from liquid to plastic behavior and from plastic to brittle rheology, respectively. The Atterberg limits are affected by both soil specific surface and soil fabric. These parameters in turn control edge and surface

Table 4  
Average properties of the analyzed cores

Core number	Water content (%)	$V_s$ (m/s)	pH	$S_s$ (m <sup>2</sup> /g)	$S_u$ (kPa)	$\rho_{\text{fluid}}$ ( $\Omega\text{m}$ )	$\rho_{\text{sed}}$ ( $\Omega\text{m}$ )	Feature
<i>Green Canyon (Bush Hill): GC185</i>								
PC07b	103.7	35.3	8.3	67.4	9.0	79.8	160.9	
PC10	108.8	25.1	8.1	–	6.0	54.8	137.2	
<i>Garden Banks mud volcano: GB425</i>								
PC 11a	51.2	32.4	–	–	6.2	60.1	152.6	Central vent
PC 12	45.1	31.9	–	–	9.9	96.7	296.2	Fluidized mud zone
PC 13	74.6	27.7	–	–	8.7	100.3	257.7	Reference
PC14	44.7	28.2	–	–	8.7	49.7	121.6	East edge of volcano
PC15	51.0	22.2	–	–	3.8	82.8	203.7	Possible current venting
PC17	50.8	20.4	7.3	–	4.4	54.0	143.8	North part of volcano
PC18 <sup>a</sup>	79.2	26.9	8.5	–	6.8	98.1	218.0	South part of volcano
PC 19 <sup>a</sup>	112.8	19.6	8.2	75.8	3.1	101.0	195.3	Reference
PC20	61.4	26.2	–	–	6.0	87.7	238.6	Mini-volcano
PC21	100.1	21.1	8.6	–	6.1	76.4	165.1	Reference
PC22	106.7	17.7	–	–	7.0	87.5	150.8	Reference
PC23	69.5	22.2	–	–	4.3	136.6	236.8	Reference
GC7	54.4	25.2	–	–	4.8	73.9	188.2	Central vent
PC24	38.2	32.7	–	–	14.2	62.4	172.6	Reference
<i>Mississippi Canyon mud mound: MC852</i>								
PC25	60.8	14.0	7.8	–	1.5	45.3	93.9	Central vent
PC26	83.7	23.7	–	–	6.3	68.4	147.6	South rim
PC27	130.1	13.9	8.7	–	3.0	102.5	214.6	South flank
PC28	99.8	14.6	8.8	–	3.7	103.8	227.0	West flank
PC29	121.5	15.2	9.2	–	4.1	95.7	195.3	East flank
PC30	64.0	18.2	8.0	52.8	4.2	43.1	88.4	Central vent

In all cases, the data shown here represent the average of values obtained at multiple locations along the length of the indicated core.  $\rho$  denotes electrical resistivity. Other symbols are as in Table 2.

<sup>a</sup> Outlying point(s) deleted.

charge, double layer thickness, and the balance between van der Waals attraction and double layer repulsion.

The lack of core samples for soil studies restricted Atterberg limit tests to only a few samples. The measured limits (ASTM D-4318 [35]) and the sediment classification based on the Unified Soil Classification System are summarized in Table 3. The CH distinction for the MC852 sediments corresponds to an inorganic clay or silt of high plasticity, while the OH or MH category for the GC185 and GB425 sediments indicates a plastic, inorganic or organic sediment of either clay or silt. These results are consistent with those obtained by [8] for a larger number of long cores obtained in various parts of the Gulf of Mexico. Taken together, the Atterberg limits, the specific surface measurements, and activity ( $=\text{(LL-PL)}/f_{200}$ , where  $f_{200}$  is the percentage of sediment passing the

#200 sieve), indicate the preponderance of illite at the three study sites.

#### 4.3. Mechanical properties

Small- and large-strain mechanical properties were determined shipboard immediately following core recovery. For the purposes of this discussion, small strain refers to measurements for which the imposed strain is less than the threshold strain, estimated at  $\sim 10^{-4}$ .

##### 4.3.1. Shear wave velocity (small strain)

The shear wave velocity in sediments is controlled by the stiffness of the granular skeleton, which in turn depends on interparticle contact forces and the degree of diagenesis. Diagenetic effects are sensitive to the strain level imposed during coring, and significant

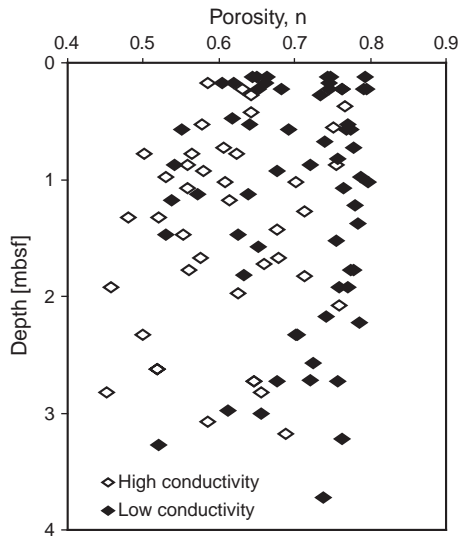


Fig. 6. Populations of sediment porosity measurements from all cores analyzed are delineated based on their electrical conductivity. The threshold for high conductivity is  $5 \text{ S m}^{-1}$  in this figure.

loss of stiffness may take place due to sampling disturbance. Interparticle contact forces in very soft fine-grained specimens are of electrical nature and proportional to interparticle distance. Therefore, porosity, pore fluid ionic content, and cementation largely control the small-strain stiffness of these sediments.

We used bender elements to attain optimal soil–transducer coupling for small-strain shear stiffness measurements. The input excitation was a square wave producing a radiated wavelet with central fre-

quency ranging from 1 kHz to 1.5 kHz. Fig. 7A and Table 4 summarize the shear wave velocity data. In all cases, sharp velocity increases along individual cores were associated with layers containing authigenic carbonate. Note that average shear wave velocities for these near-seafloor sediments were significantly lower (order of  $10^1 \text{ m/s}$ ) than values often ascribed to shallow sediments in many studies ( $>10^2 \text{ m/s}$ ).

When soil stiffness is controlled by effective stress  $\sigma'_z$ , the shear wave velocity  $V_s$  is a power function of  $\sigma'_z$ , varying as  $V_s = \alpha \sigma_z'^{\beta}$ , where  $\alpha$  and  $\beta$  denote constants [36,37]. Effective stress is calculated by integrating the sediment density between the seafloor and a given depth, assuming hydrostatic pore fluid pressure. Most cores at the Green Canyon and Mississippi Canyon sites had approximately constant shear wave velocities with depth (except near carbonates), indicating that soil stiffness is controlled either by cementation or electrical forces, not effective stress. In light of this observation and the dependence of porosity on electrical forces (Fig. 7A), we plotted the shear wave velocity with water content in Fig. 7B. The generally decreasing value of  $V_s$  with increasing water content is a characteristic behavior for high specific surface sediments at low confinement (see [38]).

#### 4.3.2. Undrained shear strength (large strain)

The undrained shear strength was determined with a pocket torvane with 3.0 kPa strength resolution using procedure ASTM D4648-94 [39]. In this proto-

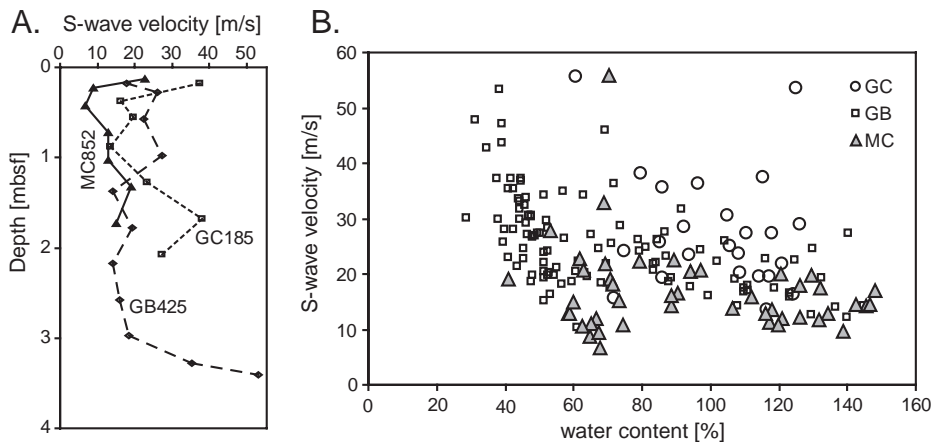


Fig. 7. (A) S-wave velocity for representative cores from each site. (B) S-wave velocity as a function of water content for the entire data set.

col, the torvane blade is pushed into the specimen and then rotated until the bulk soil fails. Under standard soil conditions, the undrained shear strength  $S_u$  of a virgin-loaded soil depends on the effective stress (e.g.,  $S_u \sim 0.2 \sigma'_v$ ) [40]. Therefore, normally consolidated soils have undrained shear strength that increases quasi-linearly with depth. This pattern was not generally present in the cores analyzed for this study. Although Table 4 shows that average undrained shear strength does tend to increase with decreasing water content, the data are too incomplete to permit a detailed analysis of causal mechanisms for this trend. Variations in effective stress, electrical forces, and/or carbonate precipitation may contribute to the observed pattern of undrained shear strength. [41] noted the occurrence of clays with water contents at or near the Atterberg liquid limit but relatively high shear strength in the upper  $\sim 7$  m of the sedimentary column at water depths less than  $\sim 330$  m on the Gulf of Mexico continental slope and attributed these characteristics to microscopic burrowing and deposition of small pyrite particles throughout the sediment matrix. While this observation may explain the characteristics of some of the cores with high water content at GC185 and GB425 (e.g., PC-07b, PC-10, PC-13, PC-22), we have no direct evidence for pyritic deposits in these cores.

#### 4.4. Electromagnetic properties

The electromagnetic properties of sediments reflect their magnetization and the ionic conduction of pore fluids. We assumed that ferromagnetic impurities were absent and thus measured only permittivity and conductivity.

##### 4.4.1. Dielectric permittivity

The permittivity  $\kappa^*$  of a material is a complex parameter expressed as the combination of the real component  $\kappa'$  and an imaginary component  $\kappa''$ :  $\kappa^* = \kappa' - j\kappa''$ . The real component  $\kappa' = \epsilon'/\epsilon_0$  depends on material polarizability and is expressed as the ratio between the real permittivity  $\epsilon'$  and permittivity of a vacuum  $\epsilon_0 = 8.85 \times 10^{-12}$  F/m. The imaginary component  $\kappa''$  combines both conduction ( $\sigma/\omega\epsilon_0$ ) and polarization ( $\epsilon''/\epsilon_0$ ) losses, where  $\epsilon''$  is the imaginary permittivity of the material,  $\sigma$  represents DC conductivity, and  $\omega$  denotes the angular frequency. The

effective AC conductivity is  $\sigma_{\text{eff}} = \kappa'' \omega \epsilon_0$ . Both real and imaginary components of  $\kappa^*$  depend on the properties of each material component and their interaction. For this study, complex permittivity was measured in the frequency range from 100 MHz to 1.0 GHz using an impedance analyzer (HP 8752A) and a coaxial termination probe (HP 85070A).

Measured permittivities as a function of frequency are shown in Fig. 8A for three representative core samples. Real permittivities decrease with increasing frequency, an observation that can be explained by the orientational polarization of free water molecules and the polarizability of hydrating water molecules around ions. The real permittivity  $\kappa'$  of sediments at microwave frequencies is determined by the orientational polarizability of water and is proportional to the volumetric water content.

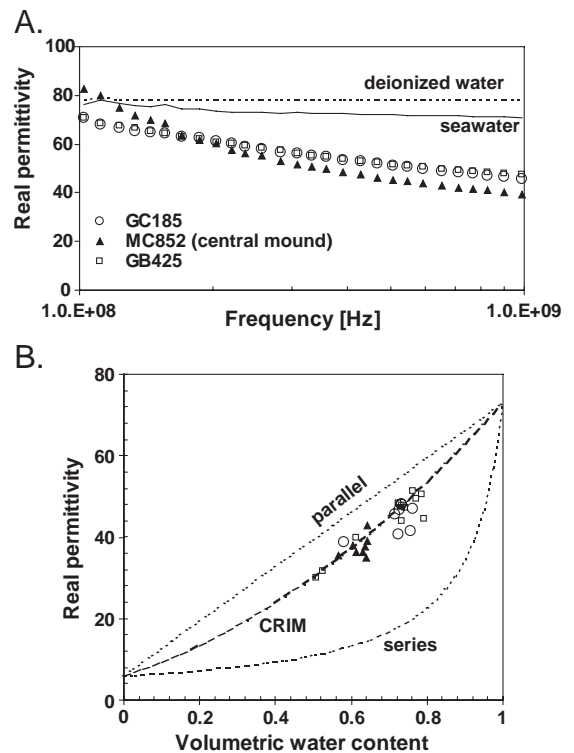


Fig. 8. (A) Complex permittivity for representative cores, plotted with values for seawater and deionized water for comparison. (B) Analysis of permittivity and water content shows that the CRIM model adequately represents the permittivity of the composite material, which lies between the upper and lower bounds predicted by the parallel or series approach.

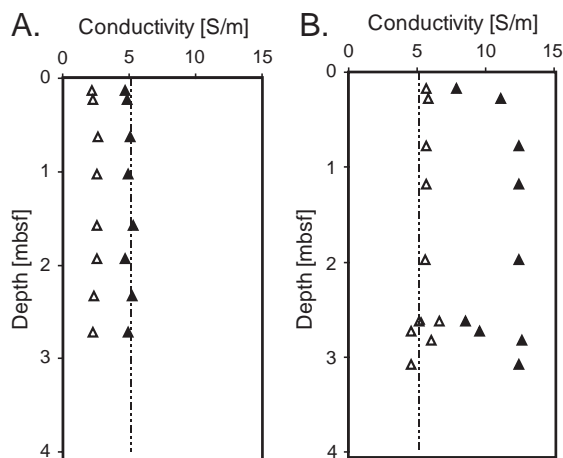


Fig. 9. Electrical conductivity of sediment ( $\Delta$ ) and pore fluid ( $\blacktriangle$ ) at locations (A) distal from vent (PC-29) and (B) close to mud volcano vent (PC-30) at MC852. The vertical dashed line indicates the electrical conductivity of seawater. Multiple points shown at  $\sim 2.6$  m depth in (B) track the evolution of pore fluid conductivity as gas hydrate dissociated, freshening the pore fluids.

The effect of volumetric water content on real permittivity is explored in Fig. 8B. The three mixture models superimposed on the figure are computed with  $\kappa_{\text{mix}}' = [n \cdot (\kappa_p')^c + (1-n) \cdot (\kappa_f')^c]^{1/c}$ , where  $\kappa_{\text{mix}}'$ ,  $\kappa_p'$ ,  $\kappa_f'$  are the real permittivity of the mixture, particles, and fluid respectively,  $n$  is the specimen porosity (equal to the volumetric water content for saturated samples), and  $c$  is a constant. This expression corresponds to the parallel arrangement model when  $c=1$ , to the series model when  $c=-1$  and the standard complex refractive index method (CRIM) for a composite dielectric when  $c=0.5$  [42]. The CRIM model, which is a volumetric model that does not take into account the microstructure of the sediments, provides the best match to the data.

#### 4.4.2. Electrical conductivity

The effective conductivity of seawater is dominated at radio and microwave frequencies by conduction losses. Therefore, the conductivity of the pore fluid,  $\sigma_{\text{el}}$  (mS/m) is related to total dissolved salts. The conductivity of the bulk sediment  $\sigma_{\text{sed}}$  is in turn related to the pore fluid conductivity  $\sigma_{\text{el}}$  through the porosity (e.g., Archie's Law). Conductivities were measured at spatial resolution of  $\sim 1$  mm using the needle probe technique described by [43].

Figs. 9 and 10 show the electrical conductivities of the pore fluid and bulk soil for cores proximal to and distal from the Mississippi Canyon mud volcano. Similar results were obtained from cores at the same positions relative to the Garden Banks mud volcano and to the Green Canyon salt dome at Bush Hill. For cores distal from the mud volcano or salt dome, pore water conductivity is constant at close to seawater values along the core (Fig. 9A). In accordance with Archie's Law predictions for these sediments, the bulk soil conductivity decreases very slightly with depth at these locations, reflecting small decreases in porosity. In regions of rapid advection near salt domes, electrical conductivity increases rapidly with depth from seawater values near the seafloor to values appropriate for brines at 1 to 2 m depth (Fig. 9B). The results presented here are independent of, yet consistent with, pore water salinity measurements reported in [6].

The high spatial resolution attainable with the needle probe electrical conductivity measurement technique permitted determination of conductivity within 1

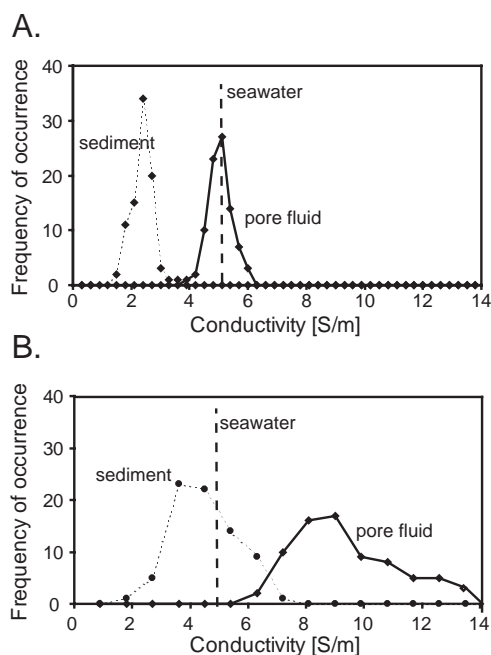


Fig. 10. Comparison of electrical conductivity values and their frequency of occurrence for all MC852 cores (A) distal from the vent and (B) close to the apparent mud volcano vent shows the more extreme (saline) conditions near the vent and the larger range of conductivities for both pore water and sediment, attesting to greater sediment heterogeneity.

mm of hydrate lenses (2.6 m depth in Fig. 9B). Measurements before dissociation showed no conductivity variation between the area immediately adjacent to the hydrate lens and the background sediment. We inferred that salts excluded during hydrate formation had diffused or been transported away, thereby homogenizing the pore waters. After hydrate dissociation, we measured locally lower conductivity values where gas hydrate had previously been present (e.g., Garden Banks at 0.7 m depth and Mississippi Canyon 2.6 m at depth).

## 5. Discussion

### 5.1. Sediment mechanical response

Interparticle forces govern the mechanical response of uncemented sediments. In the case of coarse sediments such as a sand with grain size diameter  $d$ , skeletal forces  $N$  that are proportional to effective stress  $\sigma'$  ( $N \propto \sigma' \cdot d^2$ ) prevail over other forces. In this case, the shear strength, volume change with loading, and stiffness depend on the state of effective stress, corresponding to the Coulomb criterion, Terzaghi consolidation behavior, and the Hertzian contact stiffness, respectively. On the other hand, electrical forces (double layer repulsion and van der Waals attraction) are more important than skeletal forces for small high-specific surface clay particles (small  $d$ ) at shallow depth (low  $\sigma'$ ). In this case, the soil response is sensitive to changes in pore fluid characteristics, in particular ion valence and concentration. Observed correlations between porosity and stiffness and between porosity and strength capture this indirect, causal link.

Our experimental data indicate that the strength, stiffness, and porosity of near-surface sediments in the Gulf of Mexico are not controlled by the state of effective stress. Instead, these parameters reflect changes in pore fluid ionic concentration, which can increase sharply near salt domes, fractures tapping deep fluids, and mud volcanoes. The sensitivity of near-seafloor sediments to pore fluid chemistry is consistent with their high specific surface.

Gas hydrate dissociation is expected to have at least two consequences for the overall strength of sediments. First, hydrate dissociation should increase

pore pressure as load-bearing hydrate dissociates. Second, the importance of electrical forces in maintaining the structure of clay-rich marine sediments saturated with seawater or even higher salinity fluids means that hydrate dissociation and consequent freshening of pore waters will lead to important structural changes in the sediment [44]. The increase in electrical double layer repulsion induced by the introduction of fresher waters previously bound in gas hydrate will lead to a change in clay structure from face-to-face aggregated before hydrate dissociation to dispersed structure (but still relatively high pH) after hydrate dissociation. The increase in both pore pressure and double layer repulsion and the ensuing destruction of clay skeletal structure may lead to severe loss of sediment strength.

Mousse sediment texture has been widely observed in sediments following the dissociation of gas hydrate [45–49]. The mechanistic explanation above, combined with the gas expansion that accompanies depressurization, provides a framework for understanding these textures. The relative roles of hydrate dissociation and rapid gas expansion in disturbing sediment textures and altering sediment mechanical properties are, however, difficult to separate.

### 5.2. Distribution of gas hydrates in the shallow sediments

Prior field studies observed that hydrates tend to form inside the matrix of coarse sediments, near gravel sized authigenic carbonate [1], and close to fractures and gas seeps (e.g., [18,49]). Numerical studies have explored the mechanisms for the preferential accumulation of hydrate in high permeability faults and sediments or in areas characterized by high advective rates [3,50]. Hydrates present in the cores recovered in this study were usually associated with predominantly vertical, oil-filled fractures and with coarse carbonate particles.

Disseminated hydrates were not observed within the clayey sediment matrix in recovered cores, but, as noted earlier, conditions favored the dissociation of disseminated hydrate before the core could be examined in the laboratory. The presence of disseminated gas bubbles, which alter the structure of the sediment by producing ubiquitous micro-hydraulic fractures,

combined with infrared evidence for low temperature zones (J. Weinberger, personal communication, 2002), suggested the possible presence of in situ disseminated gas hydrate.

## 6. Conclusions

Seafloor sediments were tested for geophysical and geomechanical properties at three sites in the Gulf of Mexico: Green Canyon, Garden Banks and Mississippi Canyon. The most important observations were:

- Near surface sediments were mainly composed of clay and silt particles. Values of specific surface, liquid limits, and activity indicated that clay minerals (predominantly illite) largely control sediment characteristics.
- Sediments near shallow salt domes had higher electrical conductivity (e.g., ionic concentration) and lower water content than sediments on the flanks of or distal from the domes. Pore fluid conductivity was in some cases twice the conductivity of seawater. The highly conductive pore fluids led to the dominance of interparticle electrical forces over effective stress in controlling the mechanical properties of near-seafloor sediments. The high degree of lateral variability in pore water salinity regimes in the vicinity of the mud volcanoes produced similar heterogeneity in mechanical strength. Although intuitively sediments near mud volcanoes might be expected to have lower strength and higher water content, we observe lower water content and greater salinity, both factors that lead to greater strength near the vent than in distal locations.
- Gas hydrate lenses were observed associated with oil-filled discontinuities, gas seams, and carbonate nodules within cores. Disseminated gas hydrates were not observed, but it is likely that such hydrate would have dissociated during core recovery and on-deck processing. The presence of gas bubbles and massively microfractured sediments in recovered cores in zones that had a relatively cold signature on infrared images (J. Weinberger, personal communication, 2002) suggests that disseminated hydrate may have been present in situ.
- The analysis of particle level interactions reveals a mechanistic explanation for the moussey sediment texture observed in this and other studies when hydrate dissociates in sediments. The severe loss of sediment strength upon hydrate dissociation reflects (a) the increase in pore pressure associated with the transformation of load-bearing hydrate to water and dissolved gas and (b) the destruction of clay structure due to the increase in interparticle electrical repulsion as a result of pore water freshening associated with hydrate dissociation and due to gas expansion.
- Microconductivity measurements showed that sediments adjacent to gas hydrates have similar electrical conductivity to areas distal from gas hydrates. Thus, the local increase in pore water conductivity that should accompany the exclusion of salt from the gas hydrate lattice during hydrate formation had been erased by diffusion or transport processes prior to sampling. As gas hydrate dissociated in the samples, the electrical conductivity of the sediment decreased.
- Most cores contained authigenic carbonate (ranging between 4% to 72% by weight). High anomalous strength and shear stiffness were associated with the presence of carbonates.

## Acknowledgements

We thank the crew of the *R/V Seward Johnson* for their effort to acquire samples and B. Dugan and another reviewer for comments that led to improvements in the manuscript. The cruise was conducted as part of a program funded to C.R. by National Science Foundation (NSF) grant OCE0118071. Salary for T.S.Y. was supported by the Goizueta Foundation and the Petroleum Research Fund of the American Chemical Society under grant AC38418 to J.C.S, and salary for F.F. was provided by the ChevronTexaco Joint Industry Project (JIP) under DOE grant DE-FC26-01NT41330 managed by NETL. We thank G. Dickens for the core material, J. Weinberger for acquiring thermal infrared images, Joint Oceanographic Institutions for the infrared camera, and the shipboard party for the assistance in processing cores. This research was completed while C.R. was on assignment at and wholly supported by the NSF.

The views expressed in this manuscript reflect those of the authors and not NSF, the JIP, or DOE.

## References

- [1] J.M. Brooks, M.C. Kennicutt II, R.R. Fay, T.J. McDonald, R. Sassen, Thermogenic gas hydrates in the Gulf of Mexico, *Science* 225 (1984) 409–411.
- [2] I.R. MacDonald, N.L. Guinasso, R. Sassen, J.M. Brooks, L. Lee, K.T. Scott, Gas hydrate that breaches the sea floor on the continental slope of the Gulf of Mexico, *Geology* 22 (1994) 699–702.
- [3] W. Xu, C. Ruppel, Predicting the occurrence, distribution, and evolution of methane gas hydrate in porous marine sediments from analytical models, *J. Geophys. Res.* 104 (1999) 5081–5096.
- [4] J.L. de Roo, C.J. Peters, R.N. Lichtenthaler, G.A.M. Diepen, Occurrence of methane hydrate in saturated and unsaturated solutions of sodium chloride and water in dependence of temperature and pressure, *AIChE J.* 29 (1983) 641–657.
- [5] Y.P. Handa, Effect of hydrostatic pressure and salinity on the stability of gas hydrates, *J. Phys. Chem.* 94 (1990) 2652–2657.
- [6] C. Ruppel, G.R. Dickens, D.G. Castellini, W. Gilhooly, D. Lizarralde, Heat and salt inhibition of gas hydrate in the northern Gulf of Mexico, *Geophys. Res. Lett.* 32 (2005) L04625, doi:10.1029/2004GL021909.
- [7] W.W. Sager, I.R. MacDonald, R. Hou, Geophysical signatures of mud mounds at hydrocarbon seeps on the Louisiana continental slope, northern Gulf of Mexico, *Mar. Geol.* 198 (2003) 97–132.
- [8] M.W. Johns, Geotechnical properties of Mississippi delta sediments utilizing in situ pressure sampling techniques, in: R.A. Geyer (Ed.), *Handbook of Geophysical Exploration at Sea*, CRC Press, Boca Raton, 1992, pp. 351–401.
- [9] A.G. Young, C.D. Honganen, A.J. Silva, W.R. Bryant, Comparison of geotechnical properties of large-diameter long cores and borings in deep water Gulf of Mexico, *Proc., Offshore Technol. Conf.* 12089 (2000).
- [10] A. Silva, C. Baxter, W. Bryant, A. Bradshaw, A.P. LaRosa, Stress-strain behavior and stress state of Gulf of Mexico clays in relation to slope processes, *Proc., Offshore Technol. Conf.* 12091 (2000).
- [11] G.W. Quiros, A.G. Young, J.H. Pelletier, J.H.-C. Chan, Shear strength interpretation for Gulf of Mexico clays, *Geotechnical Practice in Offshore Engineering*, ACSE Conf., 1983, pp. 144–165.
- [12] W.J. Winters, I. Nouosel, O.M. Boldina, W.F. Waite, T.D. Lorenson, C.K. Paull, W. Bryant, Physical properties of sediment related to gas hydrate in the northern Gulf of Mexico, *EOS Trans. Amer. Geophys. Union Fall Meet. Suppl.* 83 (2002) T22B–1144.
- [13] I.R. MacDonald (Ed.), *Stability and Change in Gulf of Mexico Chemosynthetic Communities*. Min. Management Serv., OCS Study MMS 2002-036, 2002, 456 pp.
- [14] C. Ruppel, M. Kinoshita, Heat, fluid, and methane flux on the Costa Rican active margin off the Nicoya Peninsula, *Earth Planet. Sci. Lett.* 179 (2000) 153–165.
- [15] W.W. Sager, C.S. Lee, I.R. MacDonald, W.W. Schroeder, High-frequency near-bottom acoustic reflection signature of hydrocarbon seeps on the Northern Gulf of Mexico continental slope, *Geo Mar. Lett.* 18 (1999) 267–276.
- [16] I.R. MacDonald, W.W. Sager, M.P. Peccini, Gas hydrate and chemosynthetic biota in mounded bathymetry at mid-slope hydrocarbon seeps: northern Gulf of Mexico, *Mar. Geol.* 18 (2003) 133–158.
- [17] F.A. Diegel, D.C. Schuster, J.F. Karlo, R.C. Shoup, P.R. Tauvers, Cenozoic structural evolution and tectono-stratigraphic framework of the Northern Gulf Coast continental margin, in: M.P.S. Jackson, D.C. Roberts, S. Snelson (Eds.), *Salt Tectonics: A Global Perspective*, AAPG Memoir, vol. 65, 1995, pp. 109–151.
- [18] T.W. Neurater, W.R. Bryant, Gas hydrates and their association with mud diapir/mud volcanoes on the Louisiana continental slope, *Proc., Offshore Technol. Conf.* 5051 (1989).
- [19] R. Sassen, S. Joye, S.T. Sweet, D.A. DeFreitas, A.V. Milkov, I.R. MacDonald, Thermogenic gas hydrates and hydrocarbon gases in complex chemosynthetic communities, Gulf of Mexico continental slope, *Org. Geochem.* 30 (1999) 485–497.
- [20] I.R. MacDonald, G.S. Boland, J.S. Baker, J.M. Brooks, M.C. Kennicutt II, R.R. Bidigare, Gulf of Mexico hydrocarbon seep communities: II. Spatial distribution of seep organisms and hydrocarbons at Bush Hill, *Mar. Biol.* 101 (1989) 235–247.
- [21] M.C. Kennicutt II, J.M. Brooks, R.R. Bidigare, G.J. Denoux, Leakage of deep, reservoirized petroleum to the near surface on the Gulf of Mexico continental slope, *Mar. Chem.* 24 (1988) 39–59.
- [22] R.D. Thomas, 3-D Multichannel seismic reflection study of variable-flux hydrocarbon seeps, continental slope, northern Gulf of Mexico, MS thesis, Texas A and M University, 2003, 66 pp.
- [23] C.R.I. Clayton, A. Siddique, R.J. Hopper, Effects of sampler design on tube sampling disturbance—numerical and analytical investigations, *Geotechnique* 48 (1998) 847–867.
- [24] E.W. Behrens, Geology of a continental slope oil seep, northern Gulf of Mexico, *Am. Assoc. Pet. Geol. Bull.* 72 (1988) 105–114.
- [25] H.H. Roberts, P. Aharon, Hydrocarbon-derived carbonate buildups of the northern Gulf of Mexico continental slope: a review of submersible investigations, *Geo Mar. Lett.* 14 (1994) 135–148.
- [26] V. Diaz-del-Rio, L. Somoza, J. Martinez-Frias, M.P. Mata, A. Delgado, F.J. Hernandez-Molina, R. Lunar, J.A. Martin-Rubi, A. Maestro, M.C. Fernandez-Puga, R. Leon, E. Llave, T. Medialdea, J.T. Vasquez, Vast fields of hydrocarbon-derived carbonate chimneys related to the accretionary wedge/olistostrome of the Gulf of Cadiz, *Mar. Geol.* 195 (2003) 177–200.
- [27] American Society for Testing and Materials, D422-63: Standard Test Method for Particle-Size Analysis of Soils, 8 pp.
- [28] J.C. Santamarina, F. Francisca, T.-S. Yun, J.-Y. Lee, A.I. Martin, C. Ruppel, Mechanical, thermal, and electrical proper-

- ties of hydrate-bearing sediments, Proc. AAPG Hedberg Conf., 2004.
- [29] J.C. Santamarina, K.A. Klein, Y.H. Wang, E. Prencke, Specific surface: determination and relevance, *Can. Geotech. J.* 39 (2002) 233–241.
- [30] J.K. Mitchell, *Fundamentals of Soil Behavior*, 2nd ed. John Wiley and Sons, New York, 1993, 473 pp.
- [31] American Society for Testing and Materials, D4373-02: Standard Test Method for Rapid Determination of Carbonate Content of Soils, 5 pp.
- [32] C. Niewohner, C. Hensen, S. Kasten, M. Zabel, H.D. Schulz, Deep sulfate reduction completely mediated by anaerobic methane oxidation in sediments of the upwelling area off Namibia, *Geochim. Cosmochim. Acta* 62 (1998) 455–464.
- [33] American Society for Testing and Materials, D2216: Standard Test Method for Laboratory Determination of Water (Moisture) Content of Soil and Rock by Mass, 5 pp.
- [34] D. Gordon, P.B. Flemings, Generation of overpressure and compaction-driven fluid flow in a Plio-Pleistocene growth-faulted basin, *Offshore Louisiana, Basin Res.* (1998) 177–196.
- [35] American Society for Testing and Materials, D4318: Standard Test Method for Liquid Limit, Plastic Limit, and Plasticity Index of Soils, 14 pp.
- [36] K.H. Stokoe, J.N.-K. Lee, S.H.-H. Lee, Characterization of soil in calibration chambers with seismic waves, in: A.B. Huang (Ed.), *Calibration Chamber Testing*, Elsevier, New York, 1991, pp. 363–376.
- [37] J.P. Sully, R.G. Campanella, Evaluation of in situ anisotropy from crosshole and downhole shear wave velocity measurements, *Geotechnique* 45 (1995) 267–282.
- [38] K. Klein, J.C. Santamarina, Soft sediments: wave based characterization, *Int. J. Geomech.* 5 (2005) 147–157, doi:10.1061/(ASCE)1532-3641(2005)5:2(147).
- [39] American Society for Testing and Materials, D4648: Standard Test Method for Laboratory Miniature Vane Shear Test for Saturated Fine-grained Clayey Soils, 7 pp.
- [40] G. Mesri, Re-evaluation of  $S_u(\text{mob})=0.22\sigma'_p$  using laboratory shear tests, *Can. Geotech. J.* 26 (1989) 162–164.
- [41] K.J. Campbell, J.R. Hooper, D.B. Prior, Engineering implications of deepwater geologic and soil conditions, Texas–Louisiana slope, Proc., *Offshore Technol. Conf.* (1986) 5105.
- [42] K. Roth, R. Schulin, H. Fluhler, W. Attinger, Calibration of time domain reflectometry for water content measurement using a composite dielectric approach, *Water Resour. Res.* 26 (1990) 2267–2273.
- [43] G.C. Cho, J.-S. Lee, J.C. Santamarina, Spatial variability in soils: high resolution assessment with electrical needle probe, *J. Geotech. Geoenviron. Eng.* 130 (2004) 843–850.
- [44] J.C. Santamarina, K.A. Klein, A. Palomino, M.S. Guimaraes, Micro-scale aspects of chemical-mechanical coupling: inter-particle forces and fabric, in: C. Di Maio, T. Hueckel, B. Loret (Eds.), *Chemo-Mechanical Coupling in Clays*, Balkema, Rotterdam, 2002.
- [45] A. Kopf, M.B. Clennell, A. Camerlenghi, Variations in sediment physical properties and permeability of mud-volcano deposits from Napoli dome and adjacent mud volcanoes, in: A.H.F. Robertson, K.-C. Emeis, C. Richter, A. Camerlenghi (Eds.), *Proc. Ocean Drill. Program Sci. Results*, vol. 160, Ocean Drilling Program, College Station, TX, 1998, pp. 625–643.
- [46] T. Lorenson, Leg 164 shipboard scientific party, graphic summary of gas hydrate occurrence by proxy measurements across the Blake Ridge, Sites 994, 995, and 997, in: C.K. Paull, et al., (Eds.), *Proc. Ocean Drill. Program Sci. Results*, vol. 164, Ocean Drilling Program, College Station, TX, 2000, pp. 247–249.
- [47] W. Soh, Computed tomography scan analysis of Site 941 cores, western mass-transport deposit, Amazon fan, in: R.D. Flood, D.J.W. Piper, A. Klaus, L.C. Peterson (Eds.), *Proc. Ocean Drill. Program Sci. Results*, vol. 155, Ocean Drilling Program, 1997, pp. 465–475.
- [48] Shipboard Scientific Party, Leg 204 summary, in: A.M. Tréhu, et al., (Eds.), *Proc. Ocean Drill. Program, Initial Rep.*, vol. 204, Ocean Drilling Program, College Station, TX, 2003, pp. 1–75.
- [49] G.D. Ginsburg, V.A. Soloviev, Methane migration within the submarine gas-hydrate stability zone under deep-water conditions, *Mar. Geol.* 137 (1997) 49–57.
- [50] J. Nimblett, C. Ruppel, Permeability evolution during formation of gas hydrates in marine sediments, *J. Geophys. Res.* 108 (2003) 2420, doi:10.1029/2001JB001650.